Electrostatic beams from tailored plasmas in a Penning–Malmberg trap

T. R. Weber, J. R. Danielson, and C. M. Surko
Department of Physics, University of California at San Diego, La Jolla, California 92093-0319, USA

In recent work, a technique was developed to extract high quality beams from single-component plasmas confined in a Penning–Malmberg trap in a 4.8 T magnetic field. In this paper, a procedure is developed to extract these beams from the confining magnetic field and then focus them to create especially tailored electrostatic beams. Electron beams are extracted from the field in two stages: they are first transported to a region of reduced field (1 mT), and then taken to zero field with a nonadiabatic, fast extraction. Once in the field-free region, the beams are focused using an Einzel lens. Experimental results and numerical simulations are presented to illustrate the extraction and focusing process. Theoretical expressions are developed to describe the modifications to the relevant beam energy and spatial distributions. Where possible, analytic expressions are presented for the case relevant here of beams with Gaussian radial profiles. Beam emittance considerations are discussed as well as prospects for further development of these techniques. Application of these techniques to provide high-quality positron beams is also discussed. © *2010 American Institute of Physics*. [doi:10.1063/1.3529370]

I. INTRODUCTION

With recent progress in antimatter research, there is a demand for high-quality positron beams.[1–5] Additionally, many other exciting positron applications lie on the horizon that will require dramatically improved antimatter beams.[6–8] Unfortunately, the rare and volatile nature of antimatter imposes severe limitations on the ability to create intense sources and specially tailored beams. Common antimatter sources are typically very weak and have large energy spreads. One tool that can be used to circumvent these impediments is the accumulation of antimatter in a Penning–Malmberg (PM) trap.[9] After filling a trap from a positron source, for example, the resulting plasmas have successfully been used as relatively bright sources of magnetized low energy positrons.[10]

We describe here a high field PM trap that can be used for the storage and manipulation of positron plasmas.[11] Plasmas are tailored using rotating electric fields [the so-called "rotating-wall" (RW) technique] to compress plasmas radially[12] and cyclotron cooling in a 4.8 T magnetic field to keep the plasma cool ($T \sim 25$ meV). Using these techniques, plasmas have been stored at high densities ($n \leq 10^{10}$) for long periods ($\tau \sim$ days).[13]

Using this device, a technique was developed to create high quality beams from the trapped nonneutral plasmas.[14–16] Those experiments and the ones described here are done with electron plasmas for increased data rate. Since it has been established that positrons can be transported efficiently from a buffer-gas trap to a UHV trap in a several Tesla field,[17] the use of electron plasmas establishes the capability to manipulate positrons in a similar manner. Using pulsed extraction from the high field, beams are created with small transverse spatial extents $\rho_b \leq 50$ μm and rms energy spreads $\Delta E \leq 30$ meV with a high degree of reproducibility.[15,16]

A current limitation on beams created in this manner is that they reside in a large magnetic field. This presents a problem for applications that require an electrostatic positron beam (i.e., a positron beam in a magnetic field-free region).[18] For example, electrostatic beams provide increased sensitivity in studying angular scattering from atomic and molecular targets,[18,19] and they have the long-term potential of developing a positron reaction microscope.[20] One can also use electrostatic techniques for additional positron beam focusing and the so-called "remoderation" to further enhance beam brightness[21,22] for applications such as Ps$_2$ and Ps-BEC formation.[7] For these applications, extraction of the beam from the magnetic field is required. However, this process presents many difficulties including a potentially dramatic increase in the beam width and mean transverse energy $\bar{E}_\perp$,[23] which is deleterious for some applications.

In a recent brief report, a technique was described to create a high-quality electrostatic beam from a PM trap.[24] Here, this technique is described in more detail, combining the experimental results with numerical simulations to illustrate the extraction and focusing processes. The initial beam is formed using the techniques presented in Ref. 15. The extraction from the field is done in two stages: the beam is first transported to a region of much lower field (1 mT), followed by a fast (i.e., nonadiabatic) extraction to zero-field. Once in this zero-field region, the beam is focused using an Einzel lens to demonstrate electrostatic-beam control and to decrease the transverse beam size while conserving the beam emittance.[25]

This paper is organized in the following manner. In Sec. II, a description is given of the experimental procedure used to extract and focus the beam and measure its properties. Section III describes the experimental results, and Sec. IV presents complementary numerical simulations. A theoretical model of the beam extraction process is presented in Sec. V that includes the modifications to the beam spatial and energy distribution functions. Presented in Sec. VI is a summary and concluding remarks, including a discussion of fu-
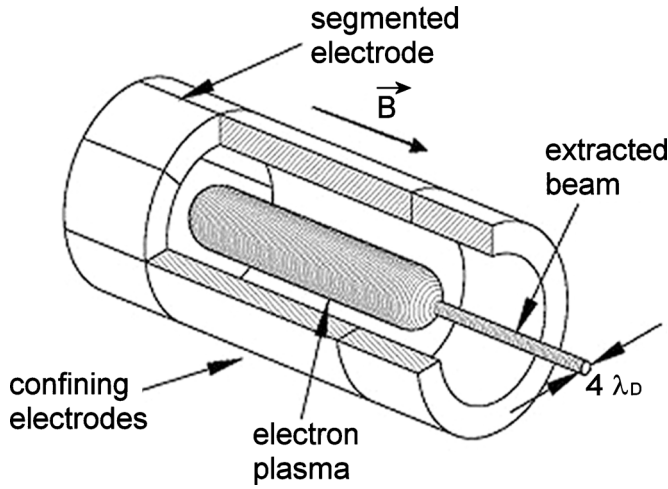
FIG. 1. Simplified schematic diagram of the technique used to extract beams with small transverse spatial extent from single-component plasmas in a Penning–Malmberg trap.

FIG. 2. (Color online) (Above) Schematic diagram of the experiment illustrating the magnetic extraction, followed by the Einzel lens spatial focus to a collector cup. (Below) The on-axis magnetic field (oriented in the z direction) $B_z(r=0)$. Saddle coils used to align the field at $z \approx 140$ cm are not shown. Reprinted from Ref. 24.

ture prospects for higher quality electrostatic beams.

II. DESCRIPTION OF THE EXPERIMENTS

The initial beam formation process in the 4.8 T field was described in Ref. 15 and is briefly reviewed here. As shown in Fig. 1, electron plasmas are formed in a Penning–Malmberg trap consisting of a cylindrical electrode structure in a uniform 4.8 T field. The magnetic field confines the particles radially, while electric fields generated from confining voltages V_C, applied to the electrodes at the ends of the plasma, confine the particles axially.

As illustrated in Fig. 1, beams are extracted from the trapped electron plasma by reducing V_C on one end of the plasma to some extraction voltage V_E in a pulsed manner ($\Delta t \sim 10 \ \mu$s) in order to allow small bursts of particles to escape. Since the plasma potential is largest at the plasma center, if V_C is lowered carefully, the beam is restricted to contain only particles from near the z axis of cylindrical symmetry. Previously, it was determined that these beams have Gaussian radial profiles [i.e., z-integrated areal particle distributions $\sigma_b(r)$] of the form[15]

$$\sigma_b(r) = \sigma_{b0} \exp[-(r/\rho_b)^2], \qquad (1)$$

where σ_{b0} is a constant and

$$\rho_b = 2\lambda_D(1+\xi)^{1/2} \qquad (2)$$

with

$$\xi = e^2 N_b / T L_p, \qquad (3)$$

the total number of beam particles per pulse N_b scaled by the plasma temperature T and length L_p. Note that although the beam width increases with ξ, for $\xi \ll 1$, $\rho_b \approx 2\lambda_D$. Thus, by controlling the temperature and density (i.e., using the RW and cyclotron cooling) beams can be formed with small transverse dimensions.

The magnetic extraction process is illustrated in Fig. 2.[24] The beam is first transported adiabatically from the 4.8 T field to 1 mT before undergoing a rapid extraction from the

field. Typical beam-transport energies are ≈ 30 eV. An important parameter used to measure the (non)adiabaticity of the process is

$$\gamma = \frac{\tau_{\text{cyc}} dB/dt}{B}, \qquad (4)$$

where τ_{cyc} is an electron gyroperiod and dB/dt is the rate of change of the magnetic field in the beam frame. Ideally, transport to low field is done in a manner such that $\gamma \ll 1$. In this case, the beam particles conserve the adiabatic invariant J defined by

$$J = \frac{E_\perp}{B}, \qquad (5)$$

where $E_\perp$ is the kinetic energy in the motion perpendicular to the magnetic field, namely, $E_\perp = 1/2 m v_\perp^2$, with $v_\perp = \sqrt{v_\theta^2 + v_r^2}$.[26] Qualitatively, during the transition to lower fields, the particles stay glued to their respective magnetic field lines while undergoing small-scale gyromotion. As illustrated in Fig. 2, the field is allowed to fall off naturally as the particles exit the high field (HF) magnet. Opposing coils (at $z \approx 150$ and 175 cm in Fig. 2) precisely define the field after the magnetic reduction and shorten the length of the experiment. Over most of the slow magnetic reduction, Eq. (5) is well satisfied, while in the last 10 cm, gamma is larger, namely, $|\gamma| = 0.6$.

One key difficulty in this experimental arrangement is aligning precisely the HF magnet with respect to the beam tube (i.e., the vacuum chamber supporting the opposing solenoid). This is accomplished by first imaging the beam on a phosphor screen temporarily mounted at the end of the low field region where the permalloy shield begins. The orientation of the HF magnet is adjustable, and it is aligned until the beam is visible on the screen. Once this is accomplished, saddle coils, placed at the beginning of the first opposing solenoid ($z \approx 140$ cm in Fig. 2), are used to center the beam in the tube.

At the end of the low field region ($z \approx 180$ cm in Fig. 2), a nonadiabatic (i.e., $\gamma \gg 1$), fast extraction is performed in which the adiabatic invariant in Eq. (5) is not conserved. In this more or less standard technique,[5] the particle has no time
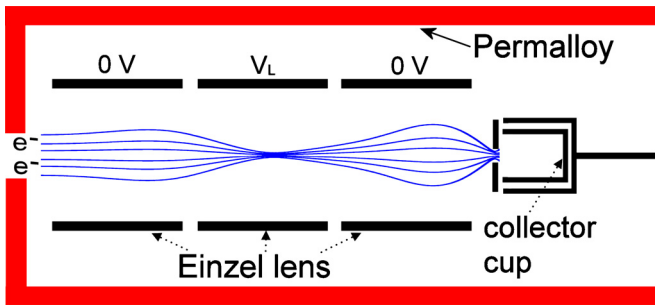
FIG. 3. (Color online) Schematic diagram of the Einzel lens and collector cup. Curves represent a sampling of beam particle trajectories calculated by the procedure described in Sec. IV. Trajectories are not to scale and only demonstrate qualitative behavior.

FIG. 4. (Color online) The initial beam in the 4.8 T field. The beam parameters are $N_b \approx 3.4 \times 10^6$, $\xi \approx 0.4$, and $\Delta E \approx 0.24$ eV. A fit to Eq. (1) is plotted (- - -), with $\rho_b \approx 65$ μm.

to respond to the $v \times B$ forces from the flaring magnetic field due to the fact that the field changes so quickly. As a result, the radial positions of the particles remain constant while they undergo an increase in the azimuthal component of their velocity v_θ from the short impulse due to the Lorentz force. This impulse is radially dependent and will by referred to later as a "kick."

Experimental details of the fast extraction are shown in Figs. 2 and 3. It is accomplished using a high magnetic permeability shield (made of sheets of Permalloy, $\mu_r \sim 2 \times 10^4$) with a front cap that has a hole in the center of diameter $d \approx 5$ cm. This hole forms a tight fit around the necked down portion of the beam tube ($z \approx 175$ cm in Fig. 2). The Permalloy screens the magnetic field from inside the shield and creates a fast extraction region at the beginning of the front-cap hole where $B = 1 \rightarrow 0$ mT.

The currents required in the two opposing coils to obtain the desired fields were initially calculated numerically using the Poisson SUPERFISH codes.[27] They were then determined more precisely by measuring the on-axis magnetic field near the shield using a Hall probe. This was necessary because the computer code could not achieve the magnetic field precision that is required (i.e., a reduction in B by a factor of $\sim 10^4$).

Inside the magnetic shield, the beam is guided only by electrostatic fields (i.e., a so-called electrostatic beam). As illustrated in Fig. 3, it is then focused with an Einzel lens and the beam properties are measured with an apertured collector cup mounted on a movable linear feedthrough. The Einzel lens consists of three identical hollow cylinders (≈ 6 cm in length and inner diameter) that are electrically isolated from the chamber and from each other. The lens is operated in an acceleration-deceleration mode where the center electrode is biased to a large positive voltage V_L and the two exterior electrodes are grounded.

Once focused, the z-integrated central beam intensity is measured with the collector cup. The aperture on the cup has a centered hole of diameter $d \approx 0.24$ cm which is used to estimate the maximum rms transverse spatial spread of the beam $\Delta r = \langle r^2 \rangle^{1/2}$. Note that for a Gaussian beam, $\Delta r = \rho_b$. By moving the collector in the z direction, the focal position of the lens is found as the position of maximum collector signal. After the approximate focal position is determined, the saddle coils are adjusted to (iteratively) maximize the signal
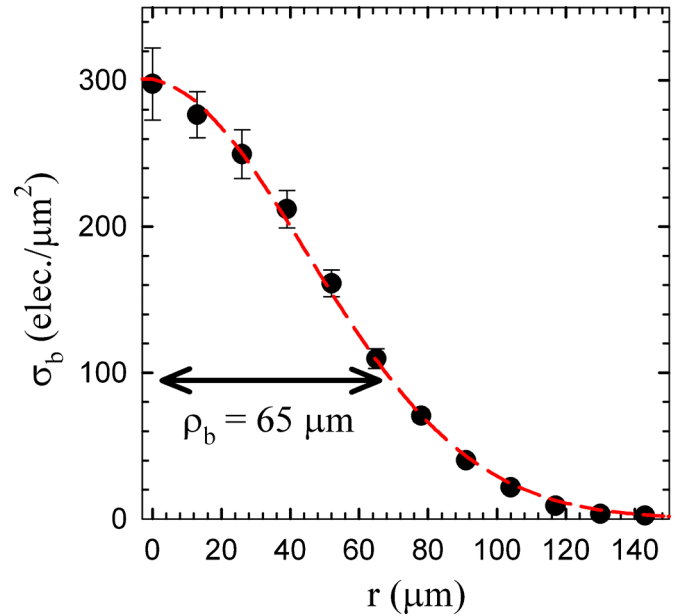
on the collector and thus precisely center the beam. This process must be repeated every few days to account for small systematic changes in the experiment. The beam-pulse intensity is also measured upstream by collecting charge on a collector plate. This measurement is used together with the collector-cup signal to obtain the percentage of the beam that passes through the collector-cup aperture.

III. EXPERIMENTAL RESULTS

Electrostatic beams were created using the experimental apparatus and procedures described in Sec. II. Figure 4 illustrates the initial radial beam distribution in the 4.8 T field. Beam pulses (≈ 5 μs in duration) were extracted from parent-plasmas with parameters, $N \approx 3.5 \times 10^8$ electrons, $n \approx 1.2 \times 10^{10}$ cm^{-3}, $T \approx 0.1$ eV, and $L_p \approx 15$ cm. The beam parameters are the number of particles per pulse $N_b \approx 3.4 \times 10^6$ and scaled beam amplitude $\xi \approx 0.4$ [cf. Eq. (3)]. The transport energy of the beam is 30 V, which is set by the plasma potential. The perpendicular energy spread is Maxwellian with $T = 0.1$ eV, while the parallel energy spread is non-Maxwellian.[16] The total rms energy spread is found to be $\Delta E \approx 0.24$ eV from previous work.[16] Inserting the relevant parameters into Eq. (2) yields a beam width $\rho_b \approx 54$ μm in the 4.8 T field, which is in reasonable agreement with the measured value of $\rho_b = 65$ μm, as shown in Fig. 4.

This beam is then extracted from the 4.8 T field in the manner described in Sec. II to produce an electrostatic beam. The adiabatic expansion of the beam, as the magnetic field is varied from B = 4.8 T to 1 mT, results in an increase in the beam radius from $\rho_b = 65$ μm to $\rho_b \approx 0.45$ cm, which remains fixed during the nonadiabatic extraction from the B field. The beam is then focused with an Einzel lens and detected using the apertured collector cup illustrated in Fig. 3.
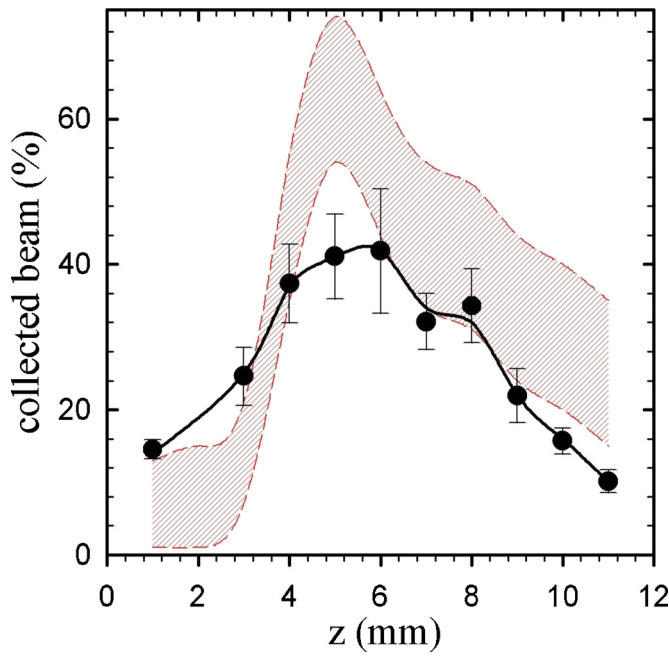
FIG. 5. (Color online) The percentage of the beam that is transmitted through the collector aperture ($d=0.24$ cm) vs the z-position of the aperture (●). Here, $V_L=5$ kV. Shown also are the predictions (shaded area) based on numerical simulations of the particle trajectories (cf. Sec. IV).

FIG. 6. (Color online) The measured focusing position of the lens vs the applied lens voltage V_L (●). Shown also are the predictions of numerical particle simulations (shaded area) described in Sec. IV.

Data for the collected beam particles as a function of the z-position of the collector aperture are plotted as solid points in Fig. 5,[24] where $z=0$ corresponds to the end of the lens ($z \approx 205$ cm in Fig. 2), and the sign convention for z is that used in Fig. 2. The data are expressed as the percentage of beam particles transmitted through the aperture at a given value of z. The voltage applied to the center electrode of the lens for this scan was $V_L=5$ kV. Operationally, we define the focus (i.e., the focal position) of the lens as the z position of maximum transmission through the aperture. For the data shown in Fig. 5, it occurs at $z \approx 5$ mm, where $\approx 43\%$ of the beam passes through the aperture of diameter $d=0.24$ cm. Note the marked asymmetry of the focusing curve as a function of z, namely, a fast rise followed by a slower decline beyond the focus. This is related to lens abberations and will be discussed further in Sec. IV.

Unfortunately, this experiment does not have the capabilities to measure a beam profile at the focal position. Because these beams are non-Gaussian (cf., Sec. IV), the only quantity that can be reported is the maximum width of the attenuated beam that passes through the collector aperture (i.e., $\Delta r < 0.12$ cm for the data shown in Fig. 5).

To study the dependence of the focusing on the lens voltage, V_L was varied from 2 to 6 kV while curves similar to those shown in Fig. 5 were measured. The focal position as a function of V_L is plotted in Fig. 6.[24] As V_L is decreased, the position of maximum focus moves farther away from the lens, while for larger values of V_L, the focus approaches the position of the end of the lens, $z=0$.

In Fig. 7, the percentage of beam particles passing through the aperture is plotted as a function of the lens voltage V_L for the same initial beam conditions as the data in Fig. 5.[24,28] The transmission rises as a function of V_L and then saturates. At $V_L=6$ kV, $\approx 55\%$ of the beam passes through the aperture.
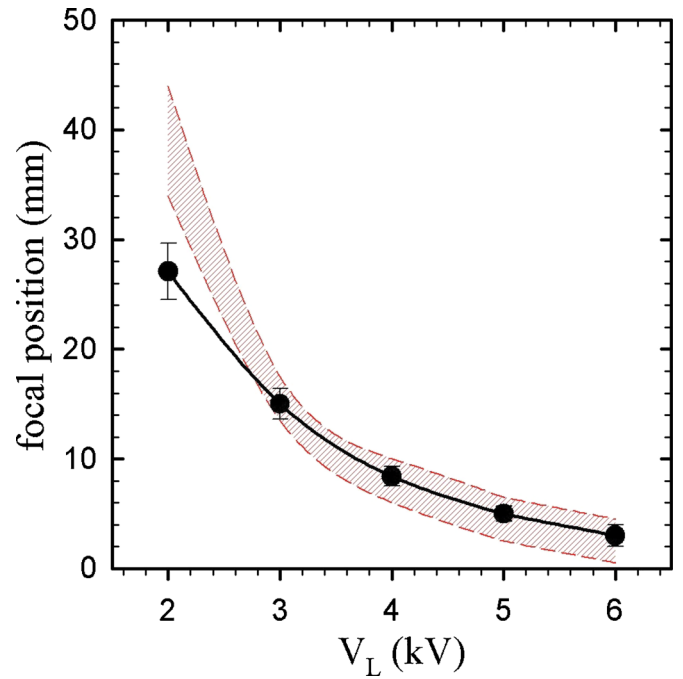
IV. NUMERICAL SIMULATIONS

In order to interpret the experimental data and extrapolate to different experimental conditions, the electron trajectories through the electric and magnetic fields during the fast
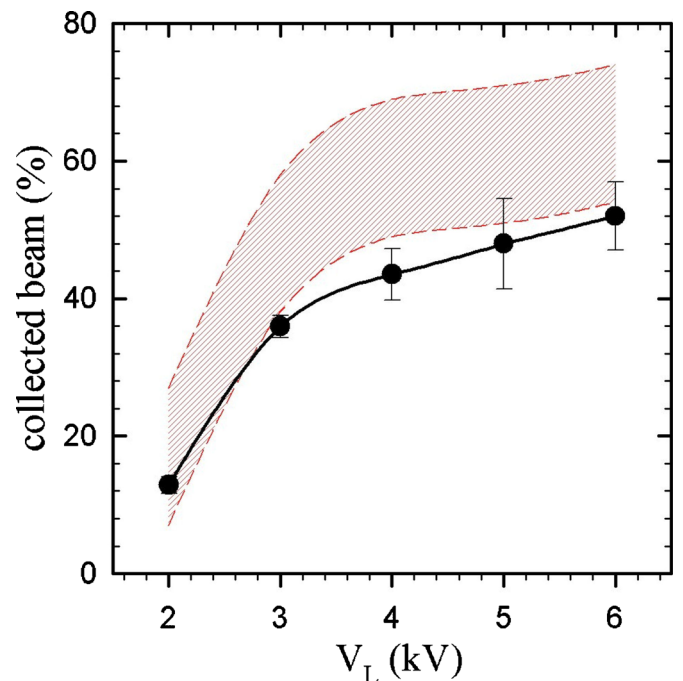
FIG. 7. (Color online) The percentage of the beam particles transmitted through the aperture vs V_L (●) for the beam shown in Fig. 4. Theoretical predictions based on the particle simulations discussed in Sec. IV are also shown (shaded area).

extraction and Einzel lens focus were simulated using numerical methods. The electric and magnetic fields are calculated from the lens, collector, permalloy, and coils (see Fig. 2) using the POISSON/SUPERFISH group of codes.[27] The assumption is made that the Gaussian beam in Fig. 4 has been slowly transported from the HF trap to 1 mT. Then, a sampling of the beam particle trajectories is calculated through the fast extraction region and Einzel lens. The percentage of beam particles passing through the aperture and focal position of the lens are estimated from these trajectories.

Three of these trajectories are plotted in Fig. 8 for two different values of V_L. Notice the scale difference in z between the two panels shown in Fig. 8. For $V_L = 5$ kV, the focus occurs at significantly smaller values of r, and across a smaller region in z, than for $V_L = 2$ kV. For a given initial radius and kick (cf. Sec. V), the minimum particle radius scales as $1/V_L$.

For all trajectories studied (ignoring aberrations, discussed below), there is a linear relation between the initial radius r_i and the minimum radius r_f. This minimum radius is set by the initial angular momentum of the particles immediately following extraction from the field, which is proportional to the δv_θ kick that they receive when exiting the magnetic field (cf., Sec. V). The smaller the kick, the closer the particles approach the z-axis at $r = 0$. The focus moves farther away from the lens as the incident beam energy is increased. This is because, at higher incoming energies, the beam particles spend less time in the lens, and hence are less affected by the focusing electric fields. For $V_L = 5$ kV, the focus is at 2, 6, and 27 cm for beam energies of 15, 30, and 60 eV, respectively.

Using the simulated trajectories, estimates of the radial beam profiles at the focus can also be obtained. Examples are shown in the insets in Fig. 8. While these estimates are noisy due to the finite number of trajectories used, they show large departures from the initial Gaussian profiles. This is primarily due to lens aberrations, namely, the fact that particles with different initial radii focus at different values of z. For $V_L = 2$ kV, the profile shows some distortion (or steepening) at the edge of the nominally Gaussian profile. However, for $V_L = 5$ kV, the distortion is much more extreme, and all the particles appear to bunch near a single radius. This can also be seen in the trajectories shown in Fig. 8(b), where between 0.5 and 0.7 mm, all the trajectories lie very close to each other. Thus, the Gaussian parameter ρ_b is no longer a good measure of the beam width at the focus. Instead, we use the rms transverse spatial spread of the beam Δr. In Fig. 8, the values for Δr are 2.0 and 1.0 mm for $V_L = 2$ and 5 kV, respectively.

The observed aberrations arise when particle trajectories pass through larger values of r in the lens (i.e., when $r \sim 0.5 R_L$, where R_L is the radius of the lens). There are two primary mechanisms for particles sampling large values of r. One is that when the particles start out at larger radii, they experience stronger radial electric fields and larger δv_θ kicks (cf. Sec. V), thus causing their trajectories to traverse larger radii in the lens. The second mechanism is due to the fact that, for large values of V_L, the large radial electric fields of the lens push particle orbits to larger radii in the lens.
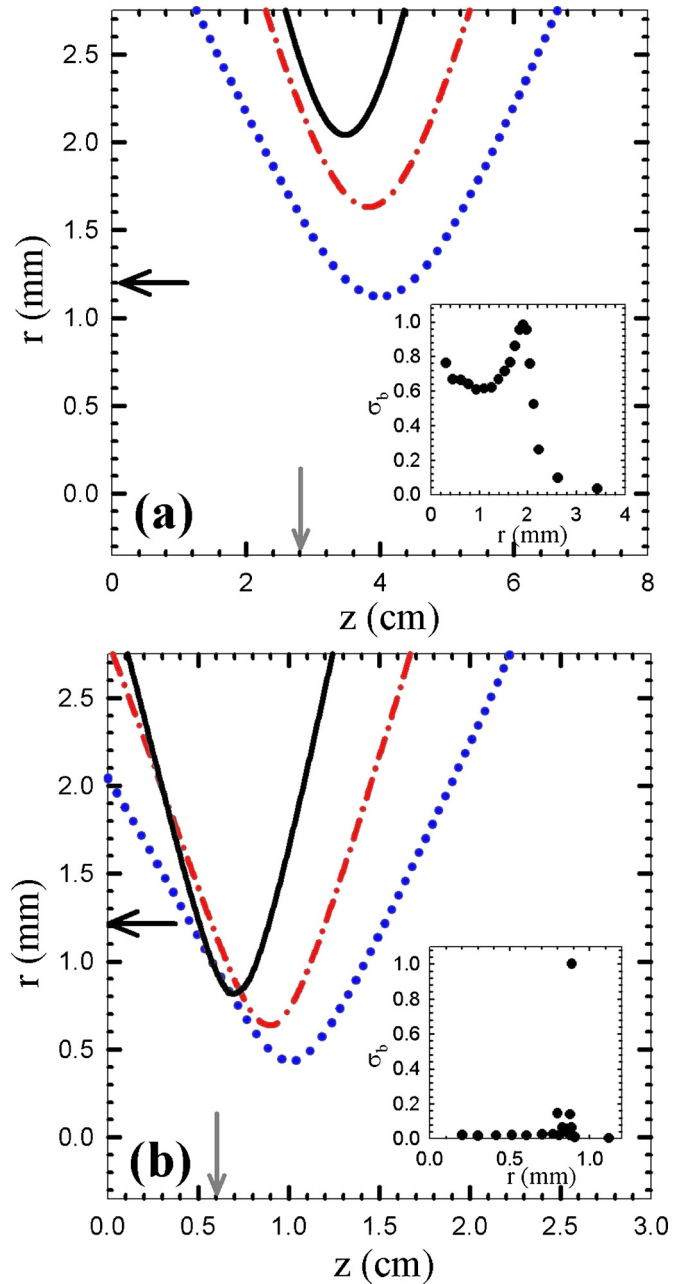
FIG. 8. (Color online) Numerically calculated particle trajectories for three different initial radii: 4 (–), 3 ($\cdot-\cdot$), and 2 mm ($\cdots$) for (a) $V_L = 2$ kV, and (b) $V_L = 5$ kV. Horizontal black arrows indicate the radial extent of the aperture used in the experiment, and vertical gray arrows indicate estimated locations of focal points, $z = 2.8$ and 0.6 cm, respectively. The insets show calculated estimates of the beam profiles [i.e., $\sigma_b(r)$, in arbitrary units] at the lens focusing position for each case.

The trajectories shown in Fig. 8 do not include effects from the collector. Including the potential surfaces of the collector makes only small changes, namely, shifting the trajectories in the z direction by a relatively small amount ($\delta z \approx -2$ mm) and increasing the minimum radius by $\approx 5\%$. When comparing the calculated trajectories to the experimental data, as described below, these collector effects were included.

Trajectories such as those shown in Fig. 8 were used to simulate the experimental data shown in Figs. 5–7. The pre-

dictions rely on knowledge of the beam profile in the 1 mT region. This quantity could only be estimated and is subject to (what turns out to be) significant error (i.e., $\rho_b = 0.45 \pm .05$ cm). One factor contributing to this uncertainty is that the orbits are not strictly adiabatic in the 10 cm or so just before the fast extraction (i.e., here $|\gamma| \sim 0.4 - 0.6$). There are also uncertainties in the exact magnetic topology at the extraction point and imperfections in the beam-transport system such as the effect of the saddle coils. Both effects would alter the beam width while the latter would additionally change the assumed Gaussian form of the beam, thus altering the predicted values.

The image of the beam on a phosphor screen near the entrance to the field-free region does indicate a moderate degree of asymmetry, implying imperfections in the beam-transport system. As a result, the exact particle trajectories (e.g., Fig. 8) show significant systematic effects based on the choice of beam radius. Although the picture remains qualitatively the same, the quantitative predictions for the number of particles making it through the collector aperture has a relatively large spread in values. Thus, we plot the theoretical predictions in Figs. 5–7 as a shaded area, representing the range of potential systematic shifts of the theoretical curves. Here, the upper and lower curves correspond, respectively, to the maximum and minimum values of ρ_b.

The experimental data and theoretical predictions are plotted in Fig. 5 and are found to be in fair agreement. Note that both the data and simulations exhibit the same asymmetry as a function of z about the focal position. This arises from the aberrations discussed above and illustrated in Fig. 8. The magnitudes at the peak disagree by $\approx 25\%$. This is likely due to misalignments in the system decreasing the maximum throughput at the focal position. Due to the dramatic field reduction and the extreme sensitivity of the lens and collector system, maintaining the alignment of the beam-line for maximum signal is difficult. Daily variations in the superconducting magnet cyrogens and small thermal expansions of the experimental apparatus have the potential to significantly alter the alignment. Other data sets have yielded data in better agreement with the numerical predictions (e.g., compare the $V_L = 5$ kV point in Fig. 7 with the maximum percentage transmission in Fig. 5).

The focal position as a function of V_L is shown in Fig. 6. With the exception of the point at $V_L = 2$ kV, the theoretical predictions are in excellent agreement with the measurements with no fitted parameters. The disagreement at 2 kV is likely due to two things. One is that the small signals and broad focusing region at small V_L create systematic difficulties in determining the position of maximum focus. The other is that, for low lens voltages, the particle simulations are very sensitive to incoming beam energy, estimated to be 30.0 eV.

The maximum collector signal as a function of V_L is shown in Fig. 7. There is a significant discrepancy between the experimental and simulated data of $\sim 20 - 30\%$. As mentioned above, this could be due to an incorrect estimate of the beam width ρ_b. As a result, the error bars on the theoretical points in Fig. 7 represent the potential range of correlated vertical shifts of the predicted data points.

To further test the experimental apparatus and model, the aperture diameter was increased to $d \approx 0.48$ cm and $\approx 80\%$ of the beam was measured to pass through the collector aperture with $V_L = 5$ kV. This agrees well with the numerical prediction from orbit calculations of $\approx 90\%$ transmission.

To summarize, there is qualitative agreement between the experiments and simulations, including the asymmetry of the collected signal versus z (Fig. 5) and the dependence of focal position on lens voltage (Fig. 6). However, the sensitivity of the trajectories to the beam radius at the extraction point results in relatively large systematic uncertainties, making more precise quantitative comparisons difficult.

V. THEORETICAL DESCRIPTION

It is difficult to construct a complete and accurate analytical model of all parts of the experiment described here. However, relatively simple models of important parts of the beam-transport and fast extraction processes can be described, and are done so here. They provide further insights, albeit some of them only qualitative (e.g., due to nonadiabatic effects and beam distortion), into the characteristics of the transported and extracted beam.

A. Single particle dynamics

Ignoring the relatively small $E \times B$ drift motion in the θ direction, the beam particles undergo cyclotron motion of radius $\rho_c \approx 1$ μm in the 4.8 T field while streaming along the magnetic field with a velocity v_z. As described in Sec. II, the first step in the extraction of a charged particle from the magnetic field is a "slow" ($\gamma < 1$) transport to 1 mT. During this process, a particle undergoes small-scale gyromotion about its magnetic field line while the guiding-center position increases as $r_f = r_i \sqrt{B_i / B_f}$ due to magnetic flux conservation. (The subscripts i and f will here and henceforth refer to the initial and final values of a quantity before and after each of the two stages of the extraction process.)

In addition to the radial position of the particle, the perpendicular and parallel energies change as well. Due to the constancy of J [cf. Eq. (5)],

$$E_{\perp f} = \frac{B_f}{B_i} E_{\perp i}, \tag{6}$$

$$E_{\|f} = E_{\|i} + E_{\perp i}\left(1 - \frac{B_f}{B_i}\right), \tag{7}$$

where $E_\|$ and $E_\perp$ are the parallel and perpendicular kinetic energies defined in Sec. II and $E_{\|f}$ is obtained from energy conservation.

After the first phase of this process, a fast extraction is performed. In this case, the magnetic field in the beam frame changes sufficiently quickly that $\gamma \gg 1$. For an ideal fast extraction, the radius of the particle remains constant as the charged particle is ripped off the field line, hence $r_f = r_i$.

In this cylindrically symmetric case, the canonical angular momentum $P_\theta = r m v_\theta - (e/c) r A_\theta$ is conserved,[25] where A_θ is the θ component of the magnetic vector potential. (Here and elsewhere in this paper, CGS units are used and the sign

of e is taken to be positive.) Using this relation, the change in v_θ ($\delta v_\theta = v_{\theta f} - v_{\theta i}$) for a fast extraction (i.e., $B \rightarrow 0$) is

$$\delta v_\theta = -\frac{eB}{2\ cm}r, \tag{8}$$

where $r = r_i = r_f$ and B is the initial magnetic field before the rapid decrease to zero. From Eq. (8), the parallel and perpendicular energies can be written as

$$E_{\perp f} = E_{\perp i} - v_{\theta i}\frac{eB}{2c}r + \frac{e^2 B^2}{8mc^2}r^2, \tag{9}$$

$$E_{\|f} = E_{\|i} + v_{\theta i}\frac{eB}{2c}r - \frac{e^2 B^2}{8mc^2}r^2, \tag{10}$$

where $E_{\|f}$ is a result of energy conservation.

B. Effect of the extraction on the beam distribution function

While Sec. A discussed the single particle dynamics during the magnetic extraction process, the beam consists of many particles with a distribution of positions and energies. Discussed here is the effect of the magnetic extraction on these distributions.

The linear scaling of initial and final radii following the slow magnetic field reduction (i.e., $r_f = r_i \sqrt{B_i / B_f}$) preserves the shape of the beam profile while rescaling the transverse dimension, namely, $\sigma_{bf}(r_f) = \sigma_{bi}(r_f \sqrt{B_f / B_i})$. In the fast extraction, the radial positions of the particles do not change (i.e., $r_f = r_i$) causing the areal density profile to also remain unchanged [i.e., $\sigma_{bf}(r) = \sigma_{bi}(r)$].

The modifications to the beam energy distribution function are more complicated. The final energy distribution after the transition to low magnetic field $f_f(E_{\|f}, E_{\perp f})$ can be obtained from the initial distribution $f_i(E_{\|i}, E_{\perp i})$ using Eqs. (6) and (7) to perform the required coordinate transformation. However, in many if not most cases, only knowledge of the mean energy and the rms energy spread is required, namely, $(\bar{E}_j \equiv \langle E_j \rangle)$ and $[\Delta E_j \equiv \sqrt{\langle (E_j - \langle E_j \rangle)^2 \rangle}]$, where j indicates the components of the $\|$, $\perp$, and total particle energy. These moments of the distribution can be calculated by averaging the appropriate function from Eqs. (6) and (7) over the original distribution f_i. This is made possible because $E_{\|f}$ and $E_{\perp f}$ are functions of $E_{\|i}$ and $E_{\perp i}$ (and $v_{\theta i}$) only.

The first moments of f_f after a slow magnetic reduction are

$$\bar{E}_{\|f} = \bar{E}_{\|i} + \bar{E}_{\perp i}\left(1 - \frac{B_f}{B_i}\right), \tag{11}$$

$$\bar{E}_{\perp f} = \bar{E}_{\perp i}\frac{B_f}{B_i}. \tag{12}$$

The second moments are

$$\Delta E_{\|f} = \sqrt{\Delta E_{\|i}^2 + \Delta E_{\perp i}^2\left(1 - \frac{B_f}{B_i}\right)^2}, \tag{13}$$

$$\Delta E_{\perp f} = \Delta E_{\perp i}\frac{B_f}{B_i}. \tag{14}$$

Although $\bar{E}_{\|f}$, $\bar{E}_{\perp f}$, $\Delta E_{\|f}$, and $\Delta E_{\perp f}$ change, the total energy $\bar{E}$ and the rms energy spread ΔE remain constant because the magnetic field does no work. The same is true for the fast magnetic extraction, described below.

Considering now the effect of the fast extraction on the energy distribution, the radial dependence of the beam distribution must be included, since Eqs. (9) and (10) depend on r. With this in mind, $f_f(E_{\|f}, E_{\perp f}, r_f)$ after the fast extraction can be obtained by another coordinate transformation, this time using Eqs. (9) and (10). However, this transformation must be performed in velocity space because v_θ appears explicitly in Eqs. (9) and (10).

Similar to the slow reduction in the field, the moments of f_f after the fast extraction are obtained by averaging functions of the quantities defined in Eqs. (9) and (10) over the original distribution function $f_i(E_{\|i}, E_{\perp i}, r_i)$. Using $\langle \ \rangle_i$ to denote this average (i.e., over $E_{\|i}$, $E_{\perp i}$, and r_i), the first moments of f_f after a fast extraction are

$$\bar{E}_{\|f} = \left\langle E_{\|i} - \frac{e^2 B^2}{8mc^2}r^2 \right\rangle_i, \tag{15}$$

$$\bar{E}_{\perp f} = \left\langle E_{\perp i} + \frac{e^2 B^2}{8mc^2}r^2 \right\rangle_i. \tag{16}$$

In Eqs. (15) and (16), we have used the fact that, for the gyromotion in the perpendicular direction considered here, $\langle v_{\theta i} \rangle_i = 0$ and $r_i = r_f = r$. The kick δv_θ transfers energy from the parallel to perpendicular direction.

The second moments of f_f after a fast extraction are

$$\Delta E_{\|f} = \left\langle \left(E_{\|i} - v_{\theta i}\frac{eB}{2c}r - \frac{e^2 B^2}{8mc^2}r^2 - \bar{E}_{\|f} \right)^2 \right\rangle_i^{1/2}, \tag{17}$$

$$\Delta E_{\perp f} = \left\langle \left(E_{\perp i} + v_{\theta i}\frac{eB}{2c}r + \frac{e^2 B^2}{8mc^2}r^2 - \bar{E}_{\perp f} \right)^2 \right\rangle_i^{1/2}. \tag{18}$$

Similar to the transition to low field, although $\bar{E}_\|$, $\bar{E}_\perp$, $\Delta E_\|$, and $\Delta E_\perp$ change, the total energy $\bar{E}$ and the rms energy spread ΔE remain constant. Now, for a given f_i, we have all the information needed to find either f_f or the first two moments of f_f following the slow reduction in, or fast extraction from, the field.

C. Results for a Gaussian radial profile and Maxwellian velocity distributions

1. Moments of the distribution function

Knowledge of the initial beam distribution function is necessary to proceed further. Previous work[15,16] described, in detail, the initial distribution functions for the beams created here. If the beam is initially formed by extraction from a plasma at temperature T and $\xi \leq 1$, the initial beam distribution function can be written as[16]

$$f_i(E_\parallel, E_\perp, r) \approx \frac{2e^{-E_\perp/T}}{T\rho_b^2} f_i(E_\parallel) \exp\left[-\left(\frac{r}{\rho_b}\right)^2\right], \quad (19)$$

where $f_i(E_\parallel)$ is written symbolically for convenience. Procedures for calculating it are described in Ref. 16 [cf. Eq. (10) and associated discussion]. Equation (19) neglects correlations between r and $E_\parallel$. These correlations are only significant in describing the fast extraction process but are negligible for the beams relevant here where $\xi < 0.5$. Where necessary, the velocity distribution function $f_i(v_z, v_\perp, r)$ can be obtained by a coordinate transformation using the expressions stated earlier.

Following the slow reduction in magnetic field, the linear scaling of the radius of each particle discussed in Sec. V A preserves the Gaussian form of Eq. (1) leading to a simple expression for the modified beam width,

$$\rho_{bf} = \sqrt{\frac{B_i}{B_f}} \rho_{bi} \quad \text{(slow extraction)}. \quad (20)$$

For the fast extraction, the radial positions of the particles do not change hence,

$$\rho_{bf} = \rho_{bi} \quad \text{(fast extraction)}. \quad (21)$$

Considering now the energy distributions, the modifications to f_i after the transition to low field or the fast extraction can be obtained by performing the coordinate transformations described in Sec. V B on Eq. (19). While this is relatively complicated, much information is contained in the low-order moments of the distributions. In particular, knowledge of only $\langle r^2 \rangle^{1/2}$, $\bar{E}_{\parallel i}$, $\bar{E}_{\perp i}$, $\Delta E_{\parallel i}$, and $\Delta E_{\perp i}$ is needed to evaluate Eqs. (11)–(18). Further, all except the moments of the parallel energy distribution are elementary, namely, $\langle r^2 \rangle^{1/2} = \rho_b$, $\bar{E}_{\perp i} = T$, and $\Delta E_{\perp i} = T$.

The quantities $\bar{E}_{\parallel i}$ and $\Delta E_{\parallel i}$ are more complicated due to plasma space-charge effects (e.g., Fig. 8 in Ref. 16). They have corrections of the order of the temperature T of the trapped plasma that depend on both the scaled beam amplitude ξ and the scaled electrode radius R_W/λ_D. For the specific case studied in Sec. III with $\xi = 0.4$ and $R_W/\lambda_D = 500$, $\bar{E}_{\parallel i} \approx |eV_E| + 3.1$ T, and $\Delta E_{\parallel i} \approx 2.2$ T (cf. Fig. 8 in Ref. 16).

For the slow reduction in magnetic field with the assumed beam distribution function in Eq. (19), the first moments are obtained by evaluating Eqs. (11) and (12),

$$\bar{E}_{\parallel f} = \bar{E}_{\parallel i} + T\left(1 - \frac{B_f}{B_i}\right), \quad (22)$$

$$\bar{E}_{\perp f} = T\frac{B_f}{B_i}. \quad (23)$$

The corresponding second moments are obtained by evaluating Eqs. (13) and (14),

$$\Delta E_{\parallel f} = \sqrt{\Delta E_{\parallel i}^2 + T^2\left(1 - \frac{B_f}{B_i}\right)^2}, \quad (24)$$

$$\Delta E_{\perp f} = T\frac{B_f}{B_i}. \quad (25)$$

Following the fast extraction (i.e., $B \to 0$), the first moments of f_f are obtained by evaluating Eqs. (15) and (16),

$$\bar{E}_{\parallel f} = |eV_E| + \bar{E}_{\parallel i} - \frac{e^2 B^2}{8mc^2}\rho_b^2, \quad (26)$$

$$\bar{E}_{\perp f} = T + \frac{e^2 B^2}{8mc^2}\rho_b^2. \quad (27)$$

The second moments of f_f for this case are similarly found using Eqs. (17) and (18) along with Eq. (19),

$$\Delta E_{\parallel f} = \sqrt{\Delta E_{\parallel i} + T\frac{e^2 B^2}{4mc^2}\rho_b^2 + \left(\frac{e^2 B^2}{8mc^2}\right)^2 \rho_b^4}, \quad (28)$$

$$\Delta E_{\perp f} = \sqrt{T^2 + T\frac{e^2 B^2}{4mc^2}\rho_b^2 + \left(\frac{e^2 B^2}{8mc^2}\right)^2 \rho_b^4}. \quad (29)$$

Here we have used the fact that, for the gyromotion in the perpendicular direction considered here, $\langle v_{\theta i}^2 \rangle_i = T/2m$ and $\langle v_{\theta i} \rangle_i = 0$. Note that Eqs. (26)–(29) refer to a fast extraction of the initial beams created here [i.e., that given by Eq. (19)]. They assume that no slow reduction of the initial beam has occurred.

2. Measure of beam quality

Once a fast extraction is performed, the beam is "electrostatic." A key measure of the quality of such a beam is the invariant emittance ϵ. To within constants of proportionality, it is defined as the product of the rms spread in radius times the rms spread in perpendicular velocities (or equivalently momenta) of the beam,[25]

$$\epsilon = \sqrt{\langle r^2 \rangle (\bar{E}_\perp)}. \quad (30)$$

In the case considered here, where the beam particles are initially in a region of nonzero magnetic field, the conservation of the canonical angular momentum results in a large increase in perpendicular velocities when the beam is extracted from the field. In this case, the relevant quantity is the so-called *generalized invariant emittance* ϵ^*. For the Gaussian radial profile and Maxwellian velocity distributions considered here, the value of $\bar{E}_\perp$ from Eq. (27) can be inserted into Eq. (30) to obtain

$$\epsilon^* = \rho_b \sqrt{T + \frac{e^2 B^2}{8mc^2}\rho_b^2}. \quad (31)$$

Note that this equation is only valid for a cylindrically symmetric case and the assumed Gaussian radial profile. A non-cylindrically symmetric system (e.g., extraction through a high-permeability grid or radial spoke arrangement) would lead to different results.

This quantity is invariant throughout the entire magnetic extraction process and reduces to the standard emittance ϵ once the beam is in the field free region. That ϵ^* is conserved during the first magnetic reduction can quickly be seen by inserting $\rho_{bf} = \rho_{bi}\sqrt{B_i/B_f}$ and $T_f = T_i(B_f/B_i)$ into Eq. (31), then noting the invariance.

While we do not find the expression of Eq. (31) for ϵ^* in the literature, it can be compared with[23]

$$\epsilon \approx \rho_b \sqrt{T} + \rho_b \sqrt{\frac{e^2 B^2}{8mc^2} \rho_b^2},$$ (32)

which was developed as an approximate expression for the fast extraction of a thermal beam from a field of strength B. The formulas are in good agreement when $T \gg e^2 B^2 \rho_b^2 / (8mc^2)$ or $T \ll e^2 B^2 \rho_b^2 / (8mc^2)$, but otherwise disagree.

Equation (31) is valid at all points during the magnetic extraction process. Thus, for the beam creation and the two-stage extraction process considered here, the emittance of the electrostatic beam is set by Eq. (31) at the point where the beam is initially created (i.e., in the 4.8 T field).

Equation (31) can also be written in the physically insightful form,

$$\epsilon^* = \rho_b \sqrt{T} \left[1 + \left(\frac{\rho_b}{2\rho_c} \right)^2 \right]^{1/2},$$ (33)

where ρ_c is the cyclotron radius, $\rho_c = \sqrt{2T/m}/(eB/mc)$. By definition, for a beam in a magnetic field, $\rho_b \gg \rho_c$. Thus, for a given T, ϵ^* is always significantly larger if the beam is born in a magnetic field. In a magnetic field of any strength, where the terms T and $e^2 B^2 / 8mc^2 \rho_b^2$ appear as above [cf. Eq. (31)], the latter term is dominant unless $\rho_b \approx \rho_c$ (i.e., the case of a weakly magnetized beam).

One of the utilities of the emittance is that it is conserved during an electrostatic focusing process. Thus, it can be used to estimate the average perpendicular beam energy $\bar{E}_\perp$ at the focal point. If a beam is focused in transverse width from ρ_{bi} to ρ_{bf}, the average perpendicular energy will change as

$$\bar{E}_{\perp f} = \bar{E}_{\perp i} \left(\frac{\rho_{bi}}{\rho_{bf}} \right)^2.$$ (34)

VI. SUMMARY AND CONCLUSIONS

Previously, we developed a technique to create high quality positron beams in a 4.8 T magnetic field by pulsed extraction from a Penning–Malmberg trap. It was demonstrated that one can use the tools available in such a UHV high-field trap, namely, rotating-wall radial plasma compression and cyclotron cooling, to tailor plasmas and improve beam quality. This paper expands on that work and describes a procedure to extract these beams from the confining magnetic field to create a class of electrostatic beams. The beams were then focused electrostatically to smaller transverse dimensions.

Table I summarizes the beam parameters during the magnetic extraction and electrostatic focusing processes for $V_L = 6$ kV, the lens voltage for which maximum focusing was achieved. Values in the first stage are those measured in the 4.8 T field. Values in the next two stages are obtained using Eqs. (20)–(29) along with energy conservation. Values in the final stage are from measurements, and the conservation of ϵ^* in Eq. (31). The value for Δr in the final stage (IV) is an upper bound for the $\approx 55\%$ of the beam that makes it

TABLE I. Beam parameters for a slow reduction from a 5 T field (I), to a 1 mT field (II), followed by a fast extraction to zero field (III), and finally focus with an Einzel lens (IV), of the beam in Fig. 4. $V_L = 6$ kV and the invariant beam emittance ϵ^* is 0.3 cm-$\sqrt{eV}$. In stages I, II, and III, the beam is Gaussian and $\Delta r = \rho_b$. See text for further details.

Stage	I	II	III	IV
B (G)	4.8×10^4	10	0	0
$\Delta E_\parallel$ (eV)	0.22	0.26	0.51	$\cdots$
$\Delta E_\perp$ (eV)	0.1	2.1×10^{-5}	0.45	$\cdots$
ΔE (eV)	0.24	0.24	0.24	0.24
$\bar{E}_\perp$ (eV)	0.1	2.1×10^{-5}	0.45	6
Δr (cm)	6.5×10^{-3}	0.45	0.45	< 0.12

through the aperture. The values for T are found from the relation $T = \bar{E}_{\perp i}$. In the focusing region, the electrical potential is found to be constant as a function of r, causing ΔE to remain unchanged from the value in stage I.

Considering the values in Table I, the fact that the initial value of $\Delta E_\parallel$ is a factor of 2 larger than the plasma temperature T is because ξ is not close to zero (i.e., $\xi = 0.4$). Working at smaller values of ξ would bring $\Delta E_\parallel$ closer to T. The increase in ρ_b during the slow extraction contrasts the relatively small increases in $\Delta E_\parallel$ and large decrease in $\Delta E_\perp$. Similarly, during the fast extraction (stage III), Δr remains constant but $\Delta E_\parallel$ and $\Delta E_\perp$ increase significantly as a result of the δv_θ kick that the particles experience when exiting the field. Beneficially, during the entire magnetic extraction and electrostatic focusing processes, ΔE remains constant. Finally, the large increase in $\bar{E}_\perp$ that occurs at the focus of the Einzel lens is a result of the conservation of the beam emittance ϵ.

At the present stage of development, the beam emittance is only roughly comparable to current cutting-edge positron beam systems. For example, using positron beams obtained directly from a buffer gas positron accumulators, values of $\epsilon^* \approx 0.12$ cm-(eV)$^{1/2}$ have been achieved in a 50 mT field.[29] However, even at this stage, the technique described here offers significant advantages in that the positrons can be accumulated and stored for long periods in UHV before delivery for a specific application. Furthermore, the transverse beam width, and hence the beam emittance, is set by the parent-plasma Debye length $\lambda_D \propto \sqrt{T/n}$. Thus, colder plasmas obtained by cooling the trapping electrodes (and hence enhancing the cyclotron cooling) and possible improvements in plasma compression techniques could be used to produce higher quality positron beams of $\epsilon^* < 0.05$. Moreover, these beams would be very cold (e.g., $\Delta E < 7$ meV) because, for small ξ, the extracted electrostatic beam maintains the initial energy spread of the parent-plasma. Thus, this technique has the potential to produce a new class of cold positron beams that are relatively ideal for spectroscopy experiments.

Considering immediate applications to positron scattering, the present electrostatic beams would be quite useful. The total energy spread of the beam is set by the parent-plasma temperature and is preserved in the extraction process. For a single particle, any change in $E_\perp$ is accompanied

by an equal and opposite change in $E_\parallel$ to conserve energy; this effect keeps ΔE constant at all times during the magnetic extraction process. Thus, the electrostatic beams created in this manner could be used in energy-spectroscopy experiments that benefit from small energy spreads. Plasmas with temperatures <20 meV have been achieved using electrodes cooled to ≈ 80 K, allowing for beams with $\Delta E < 30$ meV. These beams could be quite useful without further HF-trap improvements.

A high-permeability grid or spoke arrangement[30,31] could be used to significantly reduce the effect of the fast extraction on the particles without changing the initial magnetic field from which the beam is (fast) extracted. In essence, this would reduce the kick received by the particles upon fast extraction, thereby producing electrostatic beams with even lower emittance values.

Finally, using the procedures described here, remoderation techniques could also be used to advantage to further reduce the beam emittance. However, in this case, the energy spread will be set by the characteristics of the (re)moderator and the number of beam particles will be reduced.

ACKNOWLEDGMENTS

[1]M. Amoretti, C. Amsler, G. Bonomi, A. Bouchta, P. Bowe, C. L. Cesar, M. Charlton, M. J. T. Collier, M. Doser, V. Filippini, K. S. Fine, A. Fontana, M. C. Fujiwara, R. Funakoshi, P. Genova, J. S. Hangst, R. S. Hayano, M. H. Holzscheiter, L. V. Jrgensen, V. Lagomarsino, R. Landua, D. Lindelf, E. Lodi Rizzini, M. Macr, N. Madsen, G. Manuzio, M. Marchesotti, P. Montagna, H. Pruys, C. Regenfus, P. Riedler, J. Rochet, A. Rotondi, G. Rouleau, G. Testera, A. Variola, T. L. Watson and D. P. van der Werf, Nature (London) **419**, 456 (2002).

[2]G. Gabrielse, N. S. Bowden, P. Oxley, A. Speck, C. H. Storry, J. N. Tan, M. Wessels, D. Grzonka, W. Oelert, G. Schepers, T. Sefzick, J. Walz, H. Pittner, T. W. Hänsch, and E. A. Hessels, Phys. Rev. Lett. **89**, 233401 (2002).

[3]Y. Yamazaki, Mater. Sci. Forum **445–446**, 430 (2004).

[4]A. David, G. Kogel, P. Sperr, and W. Triftshäuser, Phys. Rev. Lett. **87**, 067402 (2001).

[5]N. Oshima, R. Suzuki, T. Ohdaira, A. Kinomura, T. Narumi, A. Uedono, and M. Fujinami, J. Appl. Phys. **103**, 094916 (2008).

[6]P. M. Platzman and A. P. Mills, Phys. Rev. B **49**, 454 (1994).

[7]A. P. Mills, Jr., D. B. Cassidy, and R. G. Greaves, Mater. Sci. Forum **445–446**, 424 (2004).

[8]T. S. Pedersen, A. H. Boozer, W. Dorland, J. P. Kremer, and R. Schmitt, J. Phys. B **36**, 1029 (2003).

[9]C. M. Surko and R. G. Greaves, Phys. Plasmas **11**, 2333 (2004).

[10]R. G. Greaves, M. D. Tinkle, and C. M. Surko, Phys. Plasmas **1**, 1439 (1994).

[11]J. R. Danielson, P. Schmidt, J. P. Sullivan, and C. M. Surko, in *Non-Neutral Plasma Physics V*, edited by M. Schauer, T. Mitchell, and R. Nebel (American Institute of Physics, Melville, NY, 2003), p. 149.

[12]J. R. Danielson and C. M. Surko, Phys. Plasmas **13**, 055706 (2006).

[13]J. R. Danielson, T. R. Weber, and C. M. Surko, Phys. Plasmas **13**, 123502 (2006).

[14]J. R. Danielson, T. R. Weber, and C. M. Surko, Appl. Phys. Lett. **90**, 081503 (2007).

[15]T. R. Weber, J. R. Danielson, and C. M. Surko, Phys. Plasmas **15**, 012106 (2008).

[16]T. R. Weber, J. R. Danielson, and C. M. Surko, Phys. Plasmas **16**, 057105 (2009).

[17]L. V. Jorgensen, M. Amoretti, G. Bonomi, P. D. Bowe, C. Canali, C. Carraro, C. L. Cesar, M. Charlton, M. Doser, A. Fontana, M. C. Fujiwara, R. Funakoshi, P. Genova, J. S. Hangst, R. S. Hayano, A. Kellerbauer, V. Lagomarsino, R. Landua, E. L. Rizzini M. Macr, N. Madsen, D. Mitchard, P. Montagna, A. Rotondi, G. Testera, A. Variola, L. Venturelli, D. P. van der Werf, and Y. Yamazaki, Phys. Rev. Lett. **95**, 025002 (2005).

[18]C. M. Surko, G. F. Gribakin, and S. J. Buckman, J. Phys. B **38**, R57 (2005).

[19]W. E. Kauppila and T. S. Stein, Adv. At., Mol., Opt. Phys. **26**, 1 (1990).

[20]J. Ullrich, R. Moshammer, A. Dorn, R. Dorner, L. Ph. H. Schmidt, and H. Schmidt-Bocking, Rep. Prog. Phys. **66**, 1463 (2003).

[21]A. P. Mills, Jr., Appl. Phys. (Berlin) **23**, 189 (1980).

[22]R. G. Greaves and C. M. Surko, Nucl. Instrum. Methods Phys. Res. B **192**, 90 (2002).

[23]V. W. Hughes, R. L. Long, M. S. Lubel, M. Posner, and W. Raith, Phys. Rev. A **5**, 195 (1972).

[24]T. R. Weber, J. R. Danielson, and C. M. Surko, "Electrostatic beams from a 5 tesla Penning-Malmberg trap," Rev. Sci. Instrum. (in press).

[25]M. Reiser, *Theory and Design of Charged Particle Beams* (Wiley, New York, 1994).

[26]J. A. Young and C. M. Surko, Nucl. Instrum. Methods Phys. Res. B **247**, 147 (2006).

[27]J. H. Billen and L. M. Young, Proceedings of the 1993 Particle Accelerator Conference, 1993, p. 790.

[28]The data point at the focal point in Fig. 5 differs slightly from that at $V_L=5$ kV in Fig. 7, likely due to run-to-run differences in the experimental conditions.

[29]D. B. Cassidy, S. H. M. Deng, R. G. Greaves, and A. P. Mills, Rev. Sci. Instrum. **77**, 073106 (2006).

[30]W. Stoeffl, P. Asoka-Kumar, and R. Howell, Appl. Surf. Sci. **149**, 1 (1999).

[31]D. Gerola, W. B. Waeber, M. Shi, and S. J. Wang, Rev. Sci. Instrum. **66**, 3819 (1995).